Realization of a multinode quantum network of remote solid-state qubits

Pompili, M.; Hermans, S. L.N.; Baier, S.; Beukers, H. K.C.; Humphreys, P. C.; Schouten, R. N.; Vermeulen, R. F.L.; Tiggelman, M. J.; Dos Santos Martins, L.; Dirkse, B.

DOI
10.1126/science.abg1919

Publication date
2021

Document Version
Final published version

Published in
Science

RESEARCH ARTICLE

QUANTUM NETWORKS

Realization of a multinode quantum network of remote solid-state qubits

M. Pompili[1,2]†, S. L. N. Hermans[1,2]†, S. Baier[1,2]†‡, H. K. C. Beukers[1,2], P. C. Humphreys[1,2]§, R. N. Schouten[1,2], R. F. L. Vermeulen[1,2], M. J. Tiggelman[1,2]¶, L. dos Santos Martins[1,2], B. Dirkse[1,2], S. Wehner[1,2], R. Hanson[1,2]*

The distribution of entangled states across the nodes of a future quantum internet will unlock fundamentally new technologies. Here, we report on the realization of a three-node entanglement-based quantum network. We combine remote quantum nodes based on diamond communication qubits into a scalable phase-stabilized architecture, supplemented with a robust memory qubit and local quantum logic. In addition, we achieve real-time communication and feed-forward gate operations across the network. We demonstrate two quantum network protocols without postselection: the distribution of genuine multipartite entangled states across the three nodes and entanglement swapping through an intermediary node. Our work establishes a key platform for exploring, testing, and developing multinode quantum network protocols and a quantum network control stack.

Future quantum networks sharing entanglement across multiple nodes (*1*, *2*) will enable a range of applications such as secure communication, distributed quantum computing, enhanced sensing, and fundamental tests of quantum mechanics (*3*–*8*). Efforts in the past decade have focused on realizing the building blocks of such a network: quantum nodes capable of establishing remote entangled links as well as locally storing, processing, and reading out quantum information.

Entanglement generation through optical channels between a pair of individually controlled qubits has been demonstrated with trapped ions and atoms (*9*–*12*), diamond nitrogen-vacancy (NV) centers (*13*, *14*), and quantum dots (*15*, *16*). In addition, a number of quantum network primitives have been explored on these elementary two-node links, including nonlocal quantum gates (*17*, *18*) and entanglement distillation (*19*). Moving these qubit platforms beyond two-node experiments has so far remained an outstanding challenge owing to the combination of several demanding requirements. Multiple high-performance quantum nodes are needed that include a communication qubit with an optical interface as well as an efficient memory qubit for storage and processing. Additionally, the individual entanglement links need to be embedded into a multinode quantum network, requiring a scalable architecture and multinode control protocols.

Here, we report on the realization and integration of all elements of a multinode quantum network: optically mediated entanglement links connected through an extensible architecture, local memory qubit and quantum logic, and real-time heralding and feed-forward operations. We demonstrate the full operation of the multinode network by running two key quantum network protocols. First, we establish Greenberger-Horne-Zeilinger (GHZ) entangled states across the three nodes. Such distributed genuine multipartite entangled states are a key ingredient for many network applications (*2*) such as anonymous transmission (*20*), secret sharing (*21*), leader election (*22*), and clock stabilization (*8*). Second, we perform entanglement swapping through an intermediary node, which is the central protocol for entanglement routing on a quantum network enabling any-to-any connectivity (*23*, *24*). Owing to efficient coherence protection on all qubits, combined with real-time feed-forward operations, these protocols are realized in a heralded fashion, delivering the final states ready for further use. This capability of heralding successful completion of quantum protocols is critical for scalability; its demonstration here presents a key advance from earlier experiments using photons (*25*) and quantum memories (*26*).

Our network is composed of three spatially separated quantum nodes (Fig. 1, A and B), labeled Alice, Bob, and Charlie. Each node consists of an NV center electronic spin as a communication qubit. In addition, the middle node Bob uses a carbon-13 nuclear spin as a memory qubit. Initialization and single-shot readout of the communication qubits are performed through resonant optical excitation and measurement of state-dependent

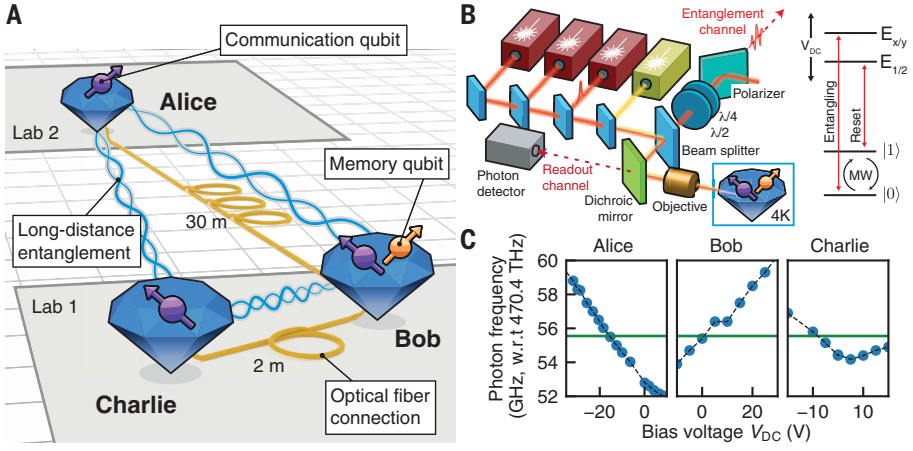

Fig. 1. The three-node quantum network. (**A**) Layout of the network. Three nodes, labeled Alice, Bob, and Charlie, are located in two separate labs. Each node contains an NV center communication qubit (purple). At Bob, an additional nuclear spin qubit (orange) is used in the presented experiments. Fiber connections between the nodes (lengths indicated) enable remote entanglement generation on the links Alice-Bob and Bob-Charlie, which, combined with local quantum logic, allow for entanglement to be shared between all nodes (wiggly lines). (**B**) On the left is a simplified schematic of the optical setup at each node [see fig. S1, table S1, and (*27*) for additional details]. On the right is a diagram of the relevant levels of the electronic spin qubit, showing optical transitions for remote entanglement generation and readout ("entangling"), qubit reset ("reset"), and resonant microwaves ("MW") for qubit control (see figs. S2 and S3 for additional details). The memory qubit at Bob is initialized, controlled, and read out via the electronic qubit (fig. S4). Optical transition frequencies are tuned via the dc bias voltages (V_{DC}). λ/2 (λ/4) is a half-waveplate (quarter-waveplate); $E_{x/y}$ and $E_{1/2}$ are electronic excited states. (**C**) Tuning of the optical "entangling" transition at each of the three nodes. The solid line is the working point, 470.45555 THz; the dashed line is a guide to the eye. w.r.t., with respect to.

[1]QuTech, Delft University of Technology, 2628 CJ Delft, Netherlands. [2]Kavli Institute of Nanoscience, Delft University of Technology, 2628 CJ Delft, Netherlands.
*Corresponding author. Email: r.hanson@tudelft.nl
†These authors contributed equally to this work.
‡Present address: Institut für Experimentalphysik, Universität Innsbruck, Technikerstraße 25, 6020 Innsbruck, Austria.
§Present address: DeepMind, London, UK.
¶Present address: QBlox, 2628 CJ Delft, Netherlands.

fluorescence (*14*). Universal quantum logic on the electronic-nuclear register is achieved through tailored microwave pulses delivered on chip (*27*). The nodes are connected through an optical fiber network for the quantum signals, as well as classical communication channels for synchronizing the control operations and relaying heralding signals (see below).

Remote entanglement generation hinges on indistinguishability between emitted photons. For NV centers in high-purity low-strain diamond devices, the optical transition frequencies show relatively minor variations (few GHz). We remove the remaining offsets by using dc Stark tuning at each node with bias fields generated on chip (Fig. 1C). We are thus able to bring the relevant optical transitions of all three nodes to the same frequency, which we choose to be the zero-bias frequency of Bob.

Establishing remote entanglement in a network architecture

To generate remote entanglement between a pair of nodes (i.e., one elementary link), a single-photon protocol is used (*28*, *29*) (Fig. 2A). The communication qubits of the nodes are each prepared in a superposition state $|\alpha\rangle = \sqrt{\alpha}|0\rangle + \sqrt{1-\alpha}|1\rangle$. At each node, pulsed optical excitation, which is resonant only for the $|0\rangle$ state, and subsequent photon emission deterministically create an entangled state between the communication qubit and the presence-absence of a photon (the flying qubit). The photonic modes from the two nodes are then interfered on a beam splitter, removing the which-path information. The beam splitter closes an effective interferometer formed by the optical excitation and collection paths. Detection of a single photon after the beam splitter heralds the state $|\psi^{\pm}\rangle \approx (|01\rangle \pm e^{i\Delta\theta}|10\rangle)/\sqrt{2}$ between the two communication qubits, where the ± sign depends on which of the two detectors clicked and Δθ is the optical phase difference between the two arms of the effective interferometer (*27*). Experimentally, this phase difference is set to a known value by stabilizing the full optical path using a feedback loop (*14*, *16*). This scheme yields states at maximum fidelity $1 - \alpha$ at a rate $\approx 2\alpha p_{\mathrm{det}}$, with p_{det} the probability that an emitted photon is detected.

Scaling this entangling scheme to multiple nodes requires each elementary link to be phase-stabilized independently (Fig. 2B), posing a number of new challenges. The different links, and even different segments of the same link, will generally be subject to diverse noise levels and spectra. Additionally, the optical power levels used are vastly different, from microwatts for the excitation path to attowatts for the single-photon heralding station, requiring different detector technologies for optimal signal detection. We solve these challenges with a hybrid phase-stabilization scheme that is scalable to an arbitrary number of nodes. We decompose the effective interferometer for each link into three independently addressable interferometers and stabilize each separately (see Fig. 2C for the Alice-Bob link; the link Bob-Charlie is phase-stabilized in an analogous and symmetric way; see figs. S5 to S8).

First, each node has its own local stabilization that uses unbalanced heterodyne phase detection (Fig. 2C, left). In comparison to the previous homodyne stabilization method (*14*), this enables us to obtain a higher bandwidth phase signal from the small part of the excitation light that is reflected from the diamond surface (≈1%) by boosting it with a strong reference-light beam at a known frequency offset. Moreover, this scheme allows for optimal rejection of the reflected excitation light by polarization selection, thus preventing excitation light from entering the single-photon path toward the heralding detectors and creating false entanglement heralding events. The measured phase signals are fed back on piezoelectric-mounted mirrors to stabilize the local interferometers.

Second, the global part of the effective interferometer (Fig. 2C, right) is stabilized by single-photon-level homodyne phase detection with feedback on a fiber stretcher: A small fraction of the strong reference-light beam is

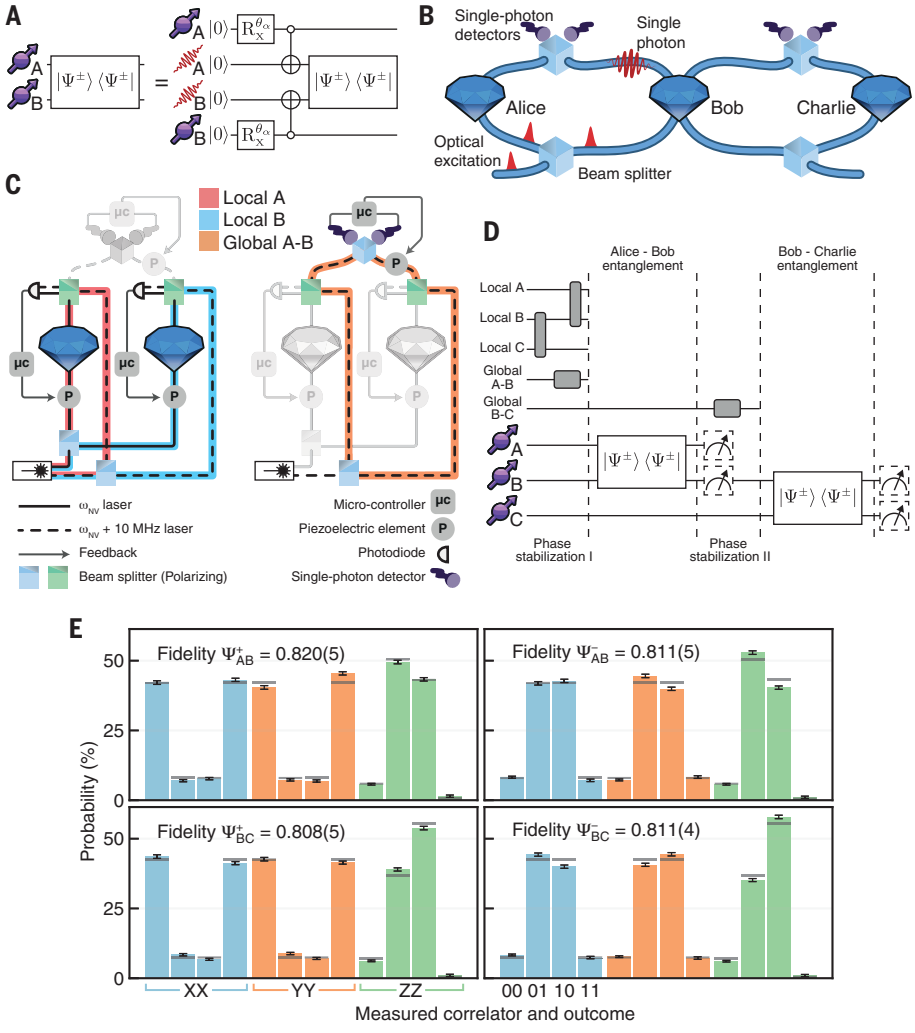

Fig. 2. Establishing remote entanglement in a network architecture. (**A**) Circuit diagram of the single-photon entanglement protocol, where $R_X^{\theta_\alpha}$ is a rotation around the *x* axis with angle θ_α, $\theta_\alpha = 2\cos^{-1}(\sqrt{\alpha})$. (**B**) Sketch of three quantum network nodes in line configuration, showing the two effective interferometers. (**C**) Phase stabilization diagram of the Alice-Bob link, highlighting the local interferometers (left) and the global interferometer (right). See (*27*) for further details. (**D**) Experimental sequence to generate Bell pairs on both Alice-Bob (A-B) and Bob-Charlie (B-C) links. Dashed boxes display measurements used in (E). (**E**) Correlation measurements on entangled states on A-B (top) and B-C (bottom) links. The left plots correspond to $|\Psi^{+}\rangle$ states; the right plots correspond to $|\Psi^{-}\rangle$ states. Shown are observed probabilities for outcomes (from left to right) 00, 01, 10, and 11 for correlation measurements in the bases XX (blue), YY (orange), and ZZ (green). Gray bars depict values from the theoretical model. Error bars indicate one standard deviation.

directed into the single-photon path, and the interference is measured using the same detectors used for entanglement generation.

This architecture provides scalability in the number of nodes and a higher feedback bandwidth compared with our previous implementation on a single link [fig. S9; see (*27*) for details]. In our current implementation, the central node—Bob—has combining optics to merge the signals coming from Alice and Charlie, so that the single-photon detectors can be shared by the two links.

Crucially, this architecture enables the successive generation of entanglement on the two elementary links as required for network protocols exploiting multinode entanglement. We benchmark its performance by running entanglement generation on both elementary links within a single experimental sequence (Fig. 2D). We achieve fidelities of the entangled Bell states exceeding 0.8 for both links (Fig. 2E), on par with the highest fidelity reported for this protocol for a single link (*14*). For the same fidelity, the entangling rates are slightly higher than in (*14*) (9 and 7 Hz for links Alice-Bob and Bob-Charlie, respectively), despite the additional channel loss from connecting the two links. The main sources of infidelity are the probability α that both nodes emit a photon, remaining optical phase uncertainty, and double excitation during the optical pulse [see table S2 and (*27*)]. A detailed physical model that includes known error sources is used here and below for comparison to the experimental data (*27*); predictions by the model are indicated by the gray bars in the correlation and fidelity plots.

Memory qubit performance and real-time feed-forward operations

To distribute entangled states across multiple nodes, generated entangled states must be stored in additional qubits while new entanglement links are created. Carbon-13 nuclear spins are excellent candidates for such memory qubits, thanks to their long coherence times, controllability, and isolation from the control drives on the electronic qubit (*30*). Recent work (*31*) indicated that their storage fidelity under network activity is mainly limited by dephasing errors resulting from the coupling to the electronic spin that is randomized on failed entanglement generation. It was suggested that the memory robustness to such errors may be further improved by operating under an increased applied magnetic field. Here, we use a magnetic field of 189 mT for our central node, as opposed to ~40 mT used in past experiments (*19*, *31*).

This higher field puts much stricter demands on the relative field stability in order to not affect the qubit frequencies; we achieve an order of magnitude reduction in field fluctuations by actively stabilizing the temperature of the sample holder, which in turn stabilizes the permanent magnet inside the cryostat (*27*). Additionally, the higher magnetic field splits the two optical transitions used for electronic spin initialization, hindering fast qubit resets; the addition of a second initialization laser, frequency locked to the first one with an offset of 480 MHz, enables us to maintain high-fidelity (>0.99) and fast (few microsecond) resets (*27*).

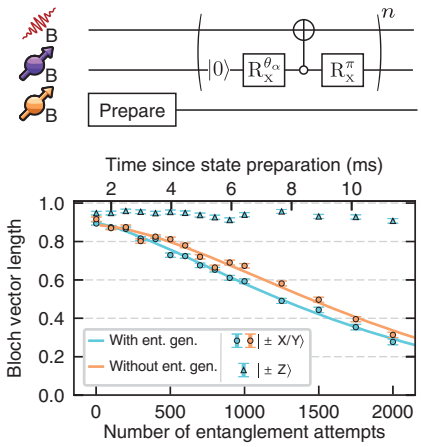

Fig. 3. Memory qubit coherence under network activity. (**Top**) Circuit diagram displaying the experimental sequence, where n is the number of entanglement attempts. (**Bottom**) Blue represents the measured Bloch vector length of memory qubit eigenstates (triangles) and superposition states (circles) versus entanglement attempts, for α = 0.05. Orange represents measured superposition decay versus time in the absence of entanglement attempts. Solid lines are fits, yielding decay constants of $N_{1/e}$ = 1843 ± 32 (2042 ± 36) with (without) entanglement generation attempts [see table S3 and (*27*) for additional details].

We measure the fidelity of stored states on Bob's memory qubit for a varying number of entanglement generation attempts (Fig. 3). The two eigenstates (±Z) do not show appreciable decay as we increase the number of entanglement generation attempts, as expected from the pure dephasing nature of the process (*31*). The superposition states degrade with an average decay constant of $N_{1/e} \approx 1800$ attempts. To gain insight into the contribution of network activity to this decay, we repeat these measurements in the absence of entanglement attempts, in which case dephasing of the memory qubit is mainly due to uncontrolled interactions with nearby nuclear spins. We find this intrinsic dephasing time to be $T_2^* = 11.6(2)$ ms, equivalent to the duration of ≈2000 entanglement generation attempts. We conclude that the intrinsic dephasing accounts for most of the decay observed under network activity, indicating the desired robustness. For the experiments discussed below, we use a timeout of 450 attempts before the sequence is restarted, as a balance between optimizing entanglement generation rate and fidelity of the stored state.

Executing protocols over quantum networks requires real-time feed-forward operations among the various nodes: Measurement outcomes at the heralding station or at nodes need to be translated into quantum gates on other nodes. We implement an asynchronous bidirectional serial communication scheme between microcontrollers at the nodes, enabling both the required timing synchronization of the nodes and the exchange of feed-forward information for the quantum network protocols (*27*). Furthermore, we integrate the feed-forward operations with local dynamical decoupling protocols that actively protect the communication qubits from decoherence. The resulting methods enable us to run multinode protocols in a heralded fashion: "Flag" signals indicate in real time the successful execution of (sub) protocols and generation of desired states that are then available for further use, thus critically enhancing the efficiency and removing the need for any postselection.

Demonstration of multinode network protocols

We now turn to the full operation of the three-node network that combines the different elements discussed above. We perform two canonical network protocols: the distribution of genuine multipartite entanglement and entanglement swapping to two non–nearest-neighbor nodes.

In both protocols, the sequence depicted in Fig. 4A is used to establish a remote entangled state on each of the two links. This sequence starts with a preparation step (depicted only in fig. S10) that synchronizes the microcontrollers of the nodes and makes sure that the NV centers in each node are in the desired charge state and in resonance with all the relevant lasers. After initialization of the memory qubit, the first entangled state is prepared on the link Alice-Bob. We interleave blocks of entanglement generation attempts with phase-stabilization cycles. Once Alice-Bob entanglement is heralded, Alice's entangled qubit is subject to a dynamical decoupling sequence while awaiting further communication from the other nodes. At Bob, deterministic quantum logic is used to swap the other half of the entangled state to the memory qubit.

The second part of the phase stabilization is then executed, followed by the generation of remote entanglement between the communication qubits of Bob and Charlie. In case of a timeout (no success within the preset number of attempts), the full protocol is restarted. In case of success, a dynamical decoupling sequence is started on Charlie's communication qubit analogous to the protocol on Alice. At Bob, a Z-rotation is applied to the memory

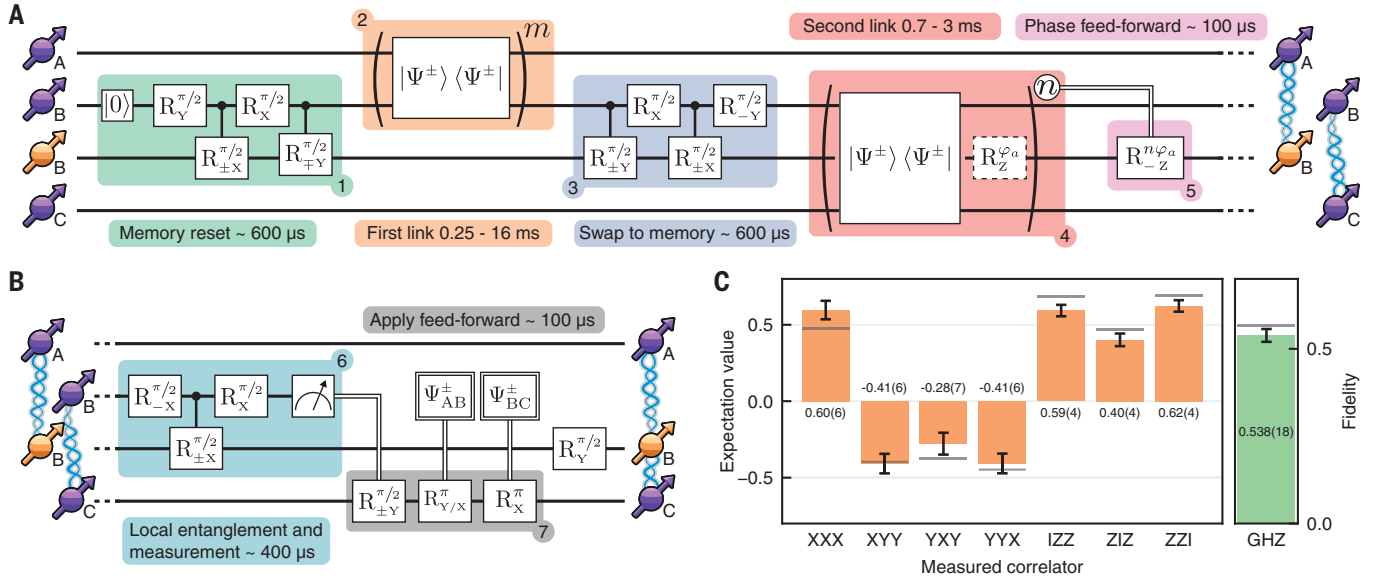

Fig. 4. Distribution of genuine multipartite entanglement across the quantum network. (**A**) Circuit diagram displaying the experimental sequence used to establish entanglement on both elementary links. (**B**) Circuit diagram displaying the experimental sequence for distributing a three-partite GHZ state across the three nodes. (**C**) Outcomes of correlation measurements and the resulting fidelity of the heralded GHZ state, demonstrating genuine multipartite entanglement. Gray bars depict values from the theoretical model. Error bars indicate one standard deviation.

qubit to compensate for the acquired phase that depends linearly on the (a priori unknown) number of entanglement attempts. This gate is implemented through an XY4 decoupling sequence on the communication qubit, with a length set in real time by the microcontroller based on which entanglement attempt was successful (*27*). After this step, the two links each share an entangled state ready for further processing: one between the communication qubit at Alice and the memory qubit at Bob and one between the communication qubits of Bob and Charlie.

The first protocol we perform is the generation of a multipartite entangled GHZ state across the three nodes. The circuit diagram describing our protocol is depicted in Fig. 4B. We first entangle the two qubits at Bob, followed by measurement of the communication qubit in a suitably chosen basis. The remaining three qubits are thereby projected into one of four possible GHZ-like states, which are all equivalent up to a basis rotation. The specific basis rotation depends both on the measurement outcome at Bob and on which Bell states ($|\Psi^+\rangle$ or $|\Psi^-\rangle$) were generated in the first part of the sequence, which in turn depends on which two photon detectors heralded the remote entangled states. These outcomes are communicated and processed in real time and the corresponding feed-forward operations are applied at Charlie. As a result, the protocol is able to achieve delivery of the same GHZ state $|\mathrm{GHZ}\rangle_{\mathrm{ABC}} = (|000\rangle + |111\rangle)/\sqrt{2}$, irrespective of the intermediate outcomes. Here, we choose to herald only on Bob reporting the $|0\rangle$ readout outcome, because the asymmetry in the communication qubit readout fidelities renders this outcome more faithful (*27*). Additionally, this choice automatically filters out events in which the NV center of Bob was in the incorrect charge state or off resonance [occurrence ≈ 10% in this experiment; see (*27*)]. With this heralding choice, the protocol delivers GHZ states at a rate of about 1/(90 s).

We extract the fidelity to the ideal GHZ state from correlation measurements by using $F = (1 + \langle IZZ\rangle + \langle ZIZ\rangle + \langle ZZI\rangle + \langle XXX\rangle - \langle XYY\rangle - \langle YXY\rangle - \langle YYX\rangle)/8$ and find F = 0.538(18) (Fig. 4C). The state fidelity above 0.5 certifies the presence of genuine multipartite entanglement distributed across the three nodes (*32*).

In this experiment, the fidelities of the entangled states on the elementary links bound the fidelity of the heralded GHZ state to about 0.66. Other relevant error sources are the dephasing of the memory qubit and accumulation of small quantum gate errors (see table S4). We emphasize that, contrary to earlier demonstrations of distributed GHZ states with photonic qubits (*25*) and ensemble-based memories (*26*) that relied on postselection, we achieve heralded GHZ state generation: A real-time heralding signal indicates the reliable delivery of the states.

The second protocol, illustrated in Fig. 5A, demonstrates entanglement swapping of the two direct links into an entangled state of the outer two nodes. Once entanglement is established on the two links as described above, the central part of the entanglement swapping is executed: Bob, the central node, performs a Bell state measurement (BSM) on its two qubits. One way to read this protocol is that the BSM induces teleportation of the state stored on Bob's memory qubit to Charlie, by consuming the entangled state shared by Bob's communication qubit and Charlie. Because the state teleported to Charlie was Bob's share of an entangled state with Alice, the teleportation establishes direct entanglement between Alice and Charlie.

After the BSM is completed, we perform a charge and resonance (CR) check on Bob to prevent heralding on events in which the NV center of Bob was in the incorrect charge state or off resonance. We note that this CR check was not used in the heralding procedure of the GHZ generation protocol because its current implementation induces decoherence on Bob's memory qubit, which is part of the final GHZ state to be delivered. To complete the entanglement swapping, feed-forward operations are performed at Charlie to account in real time for the different measurement outcomes, analogous to the previous protocol, resulting in the delivery of the Bell state $|\Phi^+\rangle_{\mathrm{AC}} = (|00\rangle + |11\rangle)/\sqrt{2}$.

We assess the performance of the entanglement swapping by measuring three two-node correlators on the generated Bell state shared by Alice and Charlie. Because the BSM is performed with local quantum logic and single-shot readout, it is (except for the CR check step) a deterministic operation. However, given the asymmetry in the readout errors as discussed above, the fidelity of the final state will

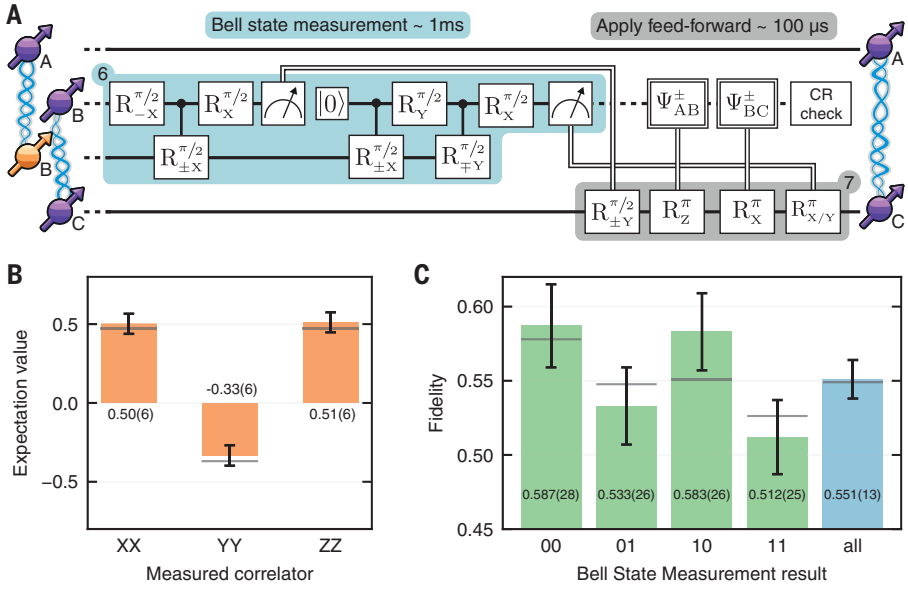

Fig. 5. Entanglement swapping on a multinode quantum network. (**A**) Circuit diagram displaying the experimental sequence for entanglement swapping, yielding an entangled state shared between the two nonconnected nodes. (**B**) Outcomes of correlation measurements on the heralded entangled state shared between Alice and Charlie for the selected Bell-state measurement outcome (see main text). (**C**) State fidelities for different outcomes of Bob's Bell-state measurement (green) and the state fidelity averaged over all outcomes (blue). In (B) and (C), gray bars depict values from the theoretical model, and error bars indicate one standard deviation.

depend on the readout outcomes. Figure 5B shows the results of the correlation measurements on the delivered state for heralding on Bob obtaining twice the outcome $|0\rangle$, yielding a state fidelity of $F = 0.587(28)$. Figure 5C compares the state fidelities across the different BSM outcomes, displaying the expected lower fidelities for outcomes of $|1\rangle$ and an average fidelity over all outcomes of $F = 0.551(13)$. The combined heralding rate is 1/(40 s). The sources of infidelity are similar to the ones discussed above (see table S5). This experiment constitutes the first demonstration of entanglement swapping from previously stored remote entangled states, enabled by the network's ability to asynchronously establish heralded elementary entanglement links, to store these entangled states, and then to efficiently consume them to teleport entanglement to distant nodes.

Conclusion and outlook

We have demonstrated the realization of a multinode quantum network. We achieved multipartite entanglement distribution across the three nodes and any-to-any connectivity through entanglement swapping. It is noteworthy that the data acquisition for the network protocols has been performed fully remotely because of the COVID-19 pandemic, highlighting the versatility and stability of our architecture. Near-term advances in the capabilities and performance of the network will be driven by further reducing the infidelities of the elementary links (*27*), by adding new subprotocols such as control methods (*30*), decoupling sequences (*31*), and repetitive readout (*33*) for the nuclear spin qubits; by improved photonic interfaces to enhance the entangling rates (*34*–*36*); and by improved control over the charge state of the NV center (*37*).

Our results open the door to exploring advanced multinode protocols and larger entangled states, for instance, by extending the local registers at the nodes. We note that a fully controlled 10-qubit register has recently been demonstrated on a similar device (*30*). Furthermore, the network provides a powerful platform for developing and testing higher-level quantum network control layers (*38*–*40*), such as the recently proposed link layer protocol for quantum networks (*41*). Quantum frequency conversion of the NV photons (*42*) can be used to interface the network nodes with deployed telecom fiber, paving the way to near-term quantum network tests over metropolitan distances. Finally, we expect the methods developed here to provide guidance for similar platforms reaching the same level of maturity in the future (*43*–*46*).

REFERENCES AND NOTES

1. H. J. Kimble, *Nature* **453**, 1023–1030 (2008).
2. S. Wehner, D. Elkouss, R. Hanson, *Science* **362**, eaam9288 (2018).
3. L. Jiang, J. M. Taylor, A. S. Sørensen, M. D. Lukin, *Phys. Rev. A* **76**, 062323 (2007).
4. A. Broadbent, J. Fitzsimons, E. Kashefi, in *Proceedings of the 2009 50th Annual IEEE Symposium on Foundations of Computer Science* (IEEE Computer Society, 2009), pp. 517–526.
5. D. Gottesman, T. Jennewein, S. Croke, *Phys. Rev. Lett.* **109**, 070503 (2012).
6. A. Ekert, R. Renner, *Nature* **507**, 443–447 (2014).
7. N. H. Nickerson, J. F. Fitzsimons, S. C. Benjamin, *Phys. Rev. X* **4**, 041041 (2014).
8. P. Kómár *et al.*, *Nat. Phys.* **10**, 582–587 (2014).
9. D. L. Moehring *et al.*, *Nature* **449**, 68–71 (2007).
10. S. Ritter *et al.*, *Nature* **484**, 195–200 (2012).
11. J. Hofmann *et al.*, *Science* **337**, 72–75 (2012).
12. L. J. Stephenson *et al.*, *Phys. Rev. Lett.* **124**, 110501 (2020).
13. H. Bernien *et al.*, *Nature* **497**, 86–90 (2013).
14. P. C. Humphreys *et al.*, *Nature* **558**, 268–273 (2018).
15. A. Delteil *et al.*, *Nat. Phys.* **12**, 218–223 (2016).
16. R. Stockill *et al.*, *Phys. Rev. Lett.* **119**, 010503 (2017).
17. P. Maunz *et al.*, *Phys. Rev. Lett.* **102**, 250502 (2009).
18. S. Daiss *et al.*, *Science* **371**, 614–617 (2021).
19. N. Kalb *et al.*, *Science* **356**, 928–932 (2017).
20. M. Christandl, S. Wehner, in *Advances in Cryptology - ASIACRYPT 2005*, B. Roy, Ed. (Lecture Notes in Computer Science Series, Springer, 2005), pp. 217–235.
21. M. Hillery, V. Bužek, A. Berthiaume, *Phys. Rev. A* **59**, 1829–1834 (1999).
22. A. Ambainis, H. Buhrman, Y. Dodis, H. Rohrig, in *Proceedings. 19th IEEE Annual Conference on Computational Complexity* (IEEE Computer Society, 2004), pp. 250–259.
23. H.-J. Briegel, W. Dür, J. I. Cirac, P. Zoller, *Phys. Rev. Lett.* **81**, 5932–5935 (1998).
24. M. Pant *et al.*, *npj Quantum Inf.* **5**, 25 (2019).
25. D. Bouwmeester, J.-W. Pan, M. Daniell, H. Weinfurter, A. Zeilinger, *Phys. Rev. Lett.* **82**, 1345–1349 (1999).
26. B. Jing *et al.*, *Nat. Photonics* **13**, 210–213 (2019).
27. Materials and methods are available as supplementary materials.
28. C. Cabrillo, J. I. Cirac, P. García-Fernández, P. Zoller, *Phys. Rev. A* **59**, 1025–1033 (1999).
29. S. Bose, P. L. Knight, M. B. Plenio, V. Vedral, *Phys. Rev. Lett.* **83**, 5158–5161 (1999).
30. C. E. Bradley *et al.*, *Phys. Rev. X* **9**, 031045 (2019).
31. N. Kalb, P. C. Humphreys, J. J. Slim, R. Hanson, *Phys. Rev. A* **97**, 062330 (2018).
32. O. Gühne, G. Tóth, *Phys. Rep.* **474**, 1–75 (2009).
33. L. Jiang *et al.*, *Science* **326**, 267–272 (2009).
34. D. Riedel *et al.*, *Phys. Rev. X* **7**, 031040 (2017).
35. E. Janitz, M. K. Bhaskar, L. Childress, *Optica* **7**, 1232–1252 (2020).
36. M. Ruf, M. J. Weaver, S. B. van Dam, R. Hanson, *Phys. Rev. Appl.* **15**, 024049 (2021).
37. S. Baier *et al.*, *Phys. Rev. Lett.* **125**, 193601 (2020).
38. R. Van Meter, *Quantum Networking* (Networks and Telecommunications Series, Wiley, 2014).
39. A. Pirker, W. Dür, *New J. Phys.* **21**, 033003 (2019).
40. W. Kozlowski, S. Wehner, in *NANOCOM '19: Proceedings of the Sixth Annual ACM International Conference on Nanoscale Computing and Communication* (Association for Computing Machinery, 2019), pp. 1–7.
41. A. Dahlberg *et al.*, in *SIGCOMM '19: Proceedings of the ACM Special Interest Group on Data Communication* (Association for Computing Machinery, 2019), pp. 159–173.
42. A. Tchebotareva *et al.*, *Phys. Rev. Lett.* **123**, 063601 (2019).
43. B. C. Rose *et al.*, *Science* **361**, 60–63 (2018).
44. C. T. Nguyen *et al.*, *Phys. Rev. Lett.* **123**, 183602 (2019).
45. M. E. Trusheim *et al.*, *Phys. Rev. Lett.* **124**, 023602 (2020).
46. N. T. Son *et al.*, *Appl. Phys. Lett.* **116**, 190501 (2020).
47. M. Pompili *et al.*, Data and software supporting "Realization of a multinode quantum network of remote solid-state qubits." 4TU.ResearchData (2021); https://doi.org/10.4121/13600589.

ACKNOWLEDGMENTS

We thank C. E. Bradley, S. Cadot, and J. van Rantwijk for experimental support and A. S. Sørensen, T. E. Northup, J. Borregaard, and T. H. Taminiau for critically reviewing the manuscript. **Funding:** We acknowledge financial support from the EU Flagship on Quantum Technologies through the project

Quantum Internet Alliance (EU Horizon 2020, grant agreement no. 820445); from the Netherlands Organisation for Scientific Research (NWO) through a VICI grant (project no. 680-47-624) and the Zwaartekracht program Quantum Software Consortium (project no. 024.003.037/3368); from the European Research Council (ERC) through an ERC Starting Grant (S.W.); and from a Consolidator Grant (grant agreement no. 772627 to R.H.) under the European Union's Horizon 2020 Research and Innovation Programme. M.P. acknowledges support from the Marie Skłodowska-Curie Actions - Nanoscale solid-state spin systems in emerging quantum technologies - Spin-NANO, grant agreement no. 676108. S.B. acknowledges support from an Erwin-Schrödinger fellowship (QuantNet, no. J 4229-N27) of the Austrian National Science Foundation (FWF). **Author contributions:** M.P., S.L.N.H., S.B., and R.H. devised the experiment. M.P., S.L.N.H., S.B., and H.K.C.B. carried out the experiments and collected the data. M.P., S.L.N.H., S.B., H.K.C.B., P.C.H., R.N.S., R.F.L.V., M.J.T., and L.d.S.M. prepared the experimental apparatus. M.P. and R.H. wrote the main manuscript with input from all authors. M.P., S.L.N.H., S.B., H.K.C.B., and R.H. wrote the supplementary materials. M.P., S.L.N.H., and S.B. analyzed the data and discussed with all authors. R.H. supervised the research. **Competing interests:** The authors declare no competing interests. **Data and materials availability:** The datasets that support this manuscript and the software to analyze them are available at 4TU.ResearchData (*47*).

SUPPLEMENTARY MATERIALS

science.sciencemag.org/content/372/6539/259/suppl/DC1
Materials and Methods
Figs. S1 to S10
Tables S1 to S5
Reference (*48*)

26 January 2021; accepted 19 March 2021
10.1126/science.abg1919

Science

Realization of a multinode quantum network of remote solid-state qubits

M. Pompili, S. L. N. Hermans, S. Baier, H. K. C. Beukers, P. C. Humphreys, R. N. Schouten, R. F. L. Vermeulen, M. J. Tiggelman, L. dos Santos Martins, B. Dirkse, S. Wehner and R. Hanson

Science **372** (6539), 259-264.
DOI: 10.1126/science.abg1919

A three-node quantum network

Future quantum networks will provide the means to develop truly secure communication channels and will have applications in many other quantum-based technologies. Pompili *et al.* present a three-node remote quantum network based on solid-state spin qubits (nitrogen-vacancy centers in diamond) coupled by photons. The implementation of two quantum protocols on the network. entanglement distribution and entanglement swapping, illustrates a key platform for exploring, testing, and developing multinode quantum networks and quantum protocols.

Science, this issue p. 259